PNAS RESEARCH ARTICLE | BIOPHYSICS AND COMPUTATIONAL BIOLOGY OPEN ACCESS

Antimicrobial peptoids pass rapidly through bacterial membranes and flocculate ribosomes and DNA: A single-cell fluorescence study

Yanyu Zhu[a,1,2,3], Josefine Eilsø Nielsen[b,c,1,4], Natalia Molchanova[d], Mainak Mustafi[a], Claudine Herlan[e], Bettina Fleck[e], Stefan Bräse[e], Ute Schepers[f], Kristian Sørensen[b], Claudia Zielke[b], Jennifer S. Lin[b], James C. Weisshaar[a], Håvard Jenssen[c], and Annelise E. Barron[b,2]

Affiliations are included on p. 10.

Edited by Ken A. Dill, Stony Brook University, Stony Brook, NY; received December 13, 2025; accepted May 20, 2026

Certain peptoids designed as mimics of host defense peptides such as LL-37 exhibit potent, broad-spectrum antibacterial, antifungal, antiparasitic, and antiviral activity with minimal cytotoxicity. Previous fixed-cell studies have suggested that the peptoids can pass through bacterial membranes and rapidly kill bacteria by aggregating intracellular macroanions, including ribosomes and DNA. However, the dynamic mechanisms of action of these biomimetic peptoids have remained elusive. We employed single-bacterial-cell, time-resolved fluorescence microscopy, and single-particle tracking methods to investigate the effects of the 12mer peptoid TM1, along with shorter alkylated and brominated analogues, on cytoplasmic membrane permeabilization and DNA and ribosome rigidification of *Escherichia coli*. Our results demonstrate that TM1 and several of its analogues permeabilize the cytoplasmic membrane within five minutes of flowing the peptoid solution over the cells—faster than seen for the important human antimicrobial peptide LL-37—and rigidify DNA and ribosomes as effectively as LL-37. Detailed biophysical structural and dynamical studies show that TM1 binds to both DNA (double-stranded and single-stranded) and single-stranded RNA in a similar manner to LL-37, which is well known to display strong nucleic acid binding. These results support our hypothesis that TM1 and its analogues exert their antimicrobial effects through intracellular aggregation of biomacromolecules such as ribosomes, RNA, and DNA. TM1 displays a higher affinity for RNA compared to DNA, suggesting it will preferentially bind in vivo to bacterial ribosomes. Our study yields insight into the dynamic effects of antimicrobial peptoids, facilitating their future development as biomimetic anti-infectives, with the additional advantage of protease invulnerability.

antimicrobial peptoid | LL-37 | antimicrobial peptide | cathelicidin | antibiotic

Significance

This study demonstrates that natural human host defense peptides such as LL-37, known to display remarkable broad-spectrum antibacterial effects and to bind to and rigidify nucleic acids, can be mimicked by simpler "peptoid" analogues (sequence- and length-specific oligo-*N*-substituted glycines). Single-cell fluorescence microscopy assays show that the precise dynamic biophysical effects of peptoids, particularly a peptoid called TM1, are quite similar to those of LL-37, and that they pass rapidly through *Escherichia coli* cell membranes and flocculate macroanions (ribosomes, DNA, RNA) inside the cell, causing them to form a rigid, semisolid form of soft matter that ceases its dynamic motion. We compare the dynamic mechanisms of action of these peptoids with natural antimicrobial peptides such as LL-37.

Antibiotic discovery and the clinical translation of novel antimicrobial agents are urgently needed to combat the emergence and spread of multidrug-resistant bacteria (1, 2). Antimicrobial peptides (AMPs) represent an essential and effective part of the innate immune systems of virtually all living organisms (3), protecting them against a broad range of pathogens. Designing drug molecules that mimic these natural peptides is therefore a promising strategy for discovering novel therapeutics. Currently there are over 30 different AMP mimics undergoing clinical trials against various infectious diseases (4). However, natural AMPs and their peptide mimics have significant limitations for clinical applications due to their rapid in vivo degradation, systemic toxicity, and high production costs (5). These issues prompted the development of sequence-specific *oligo-N-substituted glycine* (peptoid)-based AMP analogues (6). Peptoids are nonnatural peptidomimetics for which side chain substitutions occur on the amide nitrogen rather than the α-carbon (7–10). This structural difference causes peptoids to be completely protease-resistant (11) and reduces the likelihood of an immune response, in comparison to peptides. Myriad different side chains can be easily incorporated into peptoids, and as biomimetic oligomers, they are suitable for use in a vast number of biological applications including gene delivery, gene silencing, or as new anticancer and antimicrobial therapeutics (6, 7, 12–19), and are readily synthesized on an automated peptide synthesizer using an efficient solid-phase submonomer process (20).

Antimicrobial peptoid oligomers designed to mimic the physicochemical properties of AMPs have demonstrated broad-spectrum activity against both Gram-positive and Gram-negative bacteria (21–24), including antibiofilm and antiabscess activity as seen in vitro and in vivo against all *ESKAPE* pathogens (25), antipersister activity against *Pseudomonas aeruginosa* (PA) and *Staphylococcus aureus* (SA) (26), and coinfections of PA

Competing interest statement: A.E.B. is a shareholder in Maxwell Biosciences Inc.

This article is a PNAS Direct Submission.

[1]Y.Z. and J.E.N. contributed equally to this work.

[2]To whom correspondence may be addressed. Email: yanyuzhu@stanford.edu or aebarron@stanford.edu.

[3]Present address: Department of Bioengineering, Stanford University, Stanford, CA 94305.

[4]Present address: Department of Pharmacy, University of Oslo, 0371 Oslo, Norway.

This article contains supporting information online at https://www.pnas.org/lookup/suppl/doi:10.1073/pnas.2535920123/-/DCSupplemental.

Published June 29, 2026.

and SA (27), activity against viruses, including SARS-CoV-2 and HSV-1 (28, 29) and hepatitis B (30), as well as activity against fungi (31, 32) and parasites (33, 34). TM1 (previously referred to as peptoid 1) with the sequence H-(*N*Lys-*N*spe-*N*spe)$_4$-NH$_2$, where *N*Lys is *N*-(4-aminobutyl)glycine and *N*spe is *N*-(*S*)-(1-phenylethyl)glycine), is the lead compound from the first library of antimicrobial peptoids presented (6). It is a dodecameric peptoid with a simple trimer repeat that forms an amphipathic helix with one cationic face and two hydrophobic aromatic faces (22). In a recent paper we showed with small angle X-ray scattering (SAXS) that TM1 and several of its analogues included in the current work also self-assemble into defined nanostructures. TM1 forms helical bundles in aqueous solution, similarly to the human antimicrobial peptide LL-37 (25). TM1 also displays high in vivo stability (35) and excellent antimicrobial (21) and antibiofilm activity (36). Subsequently, several libraries of shorter analogues of TM1 were investigated to identify peptoids with even better selectivity and lower production costs. First, we designed and tested a series of alkylated analogues. This effort yielded TM5, an *N*tridec-1$_{4mer}$ peptoid pentamer with comparable antimicrobial activity to TM1, while displaying improved cell selectivity at significantly lower molecular weight (37). Notably, the TM5 peptoid self-assembles into ellipsoidal micelles with ~110 peptoids per micelle (25). A second library was developed featuring short, brominated analogues of TM1. These analogues contained six residues, demonstrated similar activity to TM1, and exhibited improved cytotoxicity profiles (38).

The relationship between the structures of peptoids and AMPs, and their dynamic mechanism(s) of action is still poorly understood. Cationic AMPs have been extensively studied for their ability to bind to and disrupt bacterial membranes, resulting in cell death. This may occur through lysis, or through the penetration of cell walls and subsequent interactions with intracellular targets to inhibit key metabolic processes (39–44). Investigations into mechanisms of action for tryptophan-like containing antimicrobial peptoids suggest that likely both membrane disruption and intracellular targeting are involved (45). We previously have shown by TEM and soft X-ray tomography that intracellular biomass flocculation seems to be a key mechanism of bacterial killing for several antimicrobial peptides and peptoids (46). DNA gel binding assays demonstrated that antimicrobially active peptoids bind tightly to plasmid DNA, while inactive control peptoids do not (46). In those studies, DNA binding was correlated with antibacterial activity, even while we hypothesized that other polyanionic targets in the cytoplasm might also be important. In addition, the active compounds caused rapid in vitro aggregation and flocculation of purified bacterial ribosomes (46). Recently, Kim et al. used optical diffraction tomography (ODT) to monitor the real-time morphological changes of bacteria treated with an indole side chain-containing peptoid (47). They determined that both membrane disruption and intracellular biomass flocculation were primary mechanisms of bacterial killing. Notably, nucleic acid binding of other peptoid oligomers, not designed as antimicrobials, has also been reported (13, 16, 48–50), suggesting that peptoids might also be suitable as gene delivery agents (13).

To further study the intracellular effects of antimicrobial agents, the Weisshaar lab developed a time-resolved, live-cell fluorescence microscopy technique, which enables exploration of the spatial and temporal attack of antimicrobial drug molecules on bacteria at the single-cell level (51–55). Application of this technique revealed that the cationic α-helical human peptide LL-37 (56, 57) not only permeabilizes the outer and cytoplasmic membranes (CM) of *Escherichia coli* (56, 58–61), but also induces oxidative stress (62). The foregoing single-cell imaging method has been extended to include superresolution, single-particle localization (63–65) and tracking (66–68) that allows for studying the attack of AMP on bacteria in real-time at the single molecule level. Using this technique, Zhu et al. revealed that a massive influx of LL-37 floods the *E. coli* cytoplasm, causing it to transform from its normal dynamic state into a rigidified, gel-like state that completely inhibits the proper motion of essential constituents such as chromosomal DNA and ribosome (55). The abundant, polycationic LL-37 forms a dense network of electrostatic linkages across DNA and ribosomes, rigidifying the cytoplasm and producing a physical, nonspecific shutdown of essential macromolecular dynamics (55). The polyanionic nature of the *E. coli* cytoplasm renders it highly electrostatically attractive to polycationic LL-37, making it susceptible to "electrostatic jamming" between the negatively charged biopolymer and polycationic LL-37. The binding of LL-37 was found to be reversible, but the net effect of LL-37's interactions with the cell could be effectively irreversible, potentially due to the large amount of peptide bound and the fast kinetics of the biophysical processes (55). This was discussed as a possible explanation for why only limited resistance to AMPs has been observed in bacteria, over millions of years of evolution. It is therefore of interest to determine whether these mechanisms are also operative for antimicrobial peptoids that mimic LL-37—with direct comparisons to LL-37 itself and other natural AMPs—and to study structure–activity relationships in depth, as well as the dynamics of these effects in real time.

Here, we have used the same techniques previously applied for related studies with LL-37 (55), to explore the ability of TM1 and its shorter alkylated and brominated analogues (Fig. 1), to permeabilize the CM of *E. coli*, to freeze the chromosomal loci and ribosome movement, and to compare the results quantitatively with those for natural AMPs like the already discussed LL-37, as well as Cecropin A, another linear, cationic natural antimicrobial peptide with 37 amino acids. Although it has been suggested that antimicrobial peptoids bind to plasmid DNA (45, 46), this interaction has not been extensively characterized, especially regarding single-stranded nucleic acids. Therefore, we also evaluated the binding of TM1 to DNA and RNA, conducted an in-depth study of its nucleic acid binding properties to further investigate its mechanism of bacterial killing via intracellular aggregation of biomolecules, and examined the differences between nucleic acid binding ability and structural and biophysical properties in the peptoid-DNA/RNA complexes.

Results

Self-Assembly of TM Peptoids. To characterize the self-assembled structure of the peptoids in aqueous solution we conducted synchrotron SAXS experiments and analyzed the data using theoretical modeling. Using the same approach, we recently showed that TM1, TM2, TM4, and TM6 form helical bundles in aqueous solution similarly to LL-37, while the alkylated peptoids TM5, TM8, TM9, and TM10 form core-shell ellipsoidal or wormlike micelles (25). TM7, which is not active as an antimicrobial, was the only peptoid found to have a monomeric random coil structure in this work (38). Here we present data showing that TM11, which differs from TM1 by an additional C-terminal *N*Lys, forms primarily dimeric helical bundles similarly to TM1 (*SI Appendix*, Fig. S1*A* and Table S3) with a fraction of larger bundles (20% for TM11 and 25% for TM1), which were analyzed to be trimers or tetramers. The alkylated TM15 forms core-shell ellipsoidal micelles with a core radius of 12 Å, an eccentricity (e) of 1.6 and a shell thickness of 7 Å (*SI Appendix*, Fig. S1*B* and Table S3), similarly to TM5 and TM18.

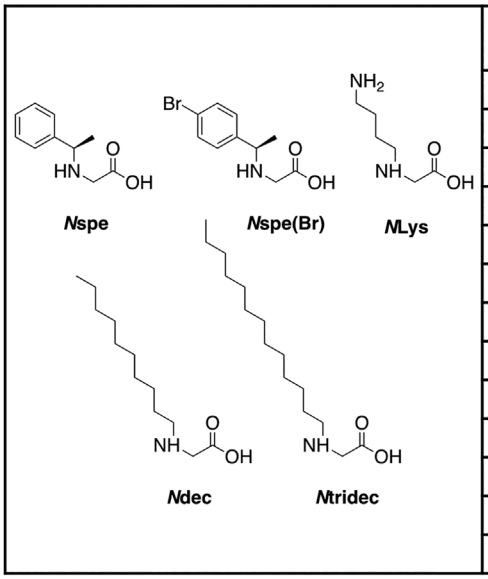

	Peptoid sequence	Mw (g/mol)	Net charge
TM1	H-(*N*Lys-*N*spe-*N*spe)$_4$-NH$_2$	1819.36	+5
TM2	H-(*N*Lys-*N*spe-*N*spe(p-Br))$_2$ -NH$_2$	1075.99	+3
TM3	H-*N*Lys-*N*spe-*N*spe-*N*Lys-*N*spe-*N*spe(p-Br)-NH$_2$	997.09	+3
TM4	H-((*N*Lys-*N*spe(p-Br)-*N*spe(p-Br))$_2$-NH$_2$	1233.78	+3
TM5	H-*N*tridec-*N*Lys-*N*spe-*N*spe-*N*Lys-NH$_2$	835.19	+3
TM6	H-(*N*Lys-*N*spe-*N*spe)$_3$ -*N*Lys-*N*spe-NH$_2$	1658.16	+5
TM7	H-(*N*Lys-*N*spe-*N*spe)$_2$-NH$_2$	918.20	+3
TM8	H-*N*dec-(*N*Lys-*N*spe-*N*spe)$_2$-NH$_2$	1115.52	+3
TM9	H-*N*dec-(*N*Lys-*N*spe-*N*spe(p-Br))$_2$-NH$_2$	1273.31	+3
TM10	H-*N*tridec-(*N*Lys-*N*spe-*N*spe(p-Br))$_2$-NH$_2$	1315.39	+2
TM11	H-(*N*Lys-*N*spe-*N*spe)$_4$-*N*Lys-NH$_2$	1946.2	+6
TM15	H-*N*tridec-*N*Lys-*N*spe-*N*spe-*N*Lys-*N*Lys-NH$_2$	963.37	+4
TM18	H-*N*dec-(*N*Lys-*N*spe-*N*spe)$_2$-*N*Lys-NH$_2$	1401.49	+4

Fig. 1. Structures of TM1 and its analogues, for full chemical structures see ref. 25.

Freezing of Chromosomal Loci Movement by Peptoids. The chromosomal DNA of *E. coli* is a long, circular biopolymer, confined by the cell envelope to a volume much smaller than its natural size (69–71). On a timescale of ~100 s, the displacement of small segments of the DNA polymer is constrained by attachment within the polymer chain (68, 72). Instead of free diffusion, the local motion is a type of subdiffusion (55, 73–75).

To characterize the local dynamics of chromosomal DNA before and after treatment with 1× the minimal inhibitory concentration (MIC) of the peptoids, we tracked the DNA locus *Right 2* labeled by the fusion protein ParB-GFP (strain JCW154, details on strain in *SI Appendix*, Table S1) (72). The labeled ParB-GFP protein polymerizes specifically at a *parS* site engineered into the chromosome near the locus *Right 2*, forming bright puncta that can be tracked without extensive photobleaching for some 600 frames with an exposure time of 50 ms/frame at a laser intensity of ~100 W/cm^2 at the sample plane (52, 55, 67).

Live *E. coli* cells were immobilized on a polylysine coated microfluidic device that enabled us to image the cell at different time points after flowing in the peptoids (76). To monitor the evolution of DNA dynamics over time, we acquired data in a series of consecutive 10-min imaging windows by recording 600-frame movie (1 s/frame) for each window following the injection of the peptoid at time t = 0. For each 10-min window, all trajectories from all cells were used to calculate a population-averaged Mean-Squared Displacement (MSD). A single apparent diffusion coefficient (D_{app}), representing the average DNA mobility during that specific time period, was then determined from a linear fit to the first 10 points of this MSD curve (see *Materials and Methods* for details).

Fig. 2 *A–D* display the time dependence of D_{app} after flowing peptoid into the microfluidic channel. On these time-course plots, each single D_{app} value is plotted at the midpoint of its corresponding 10-min imaging window. For instance, the first data point for TM2 (Fig. 2*D*) with an *x-axis* value of 6 min indicates that, during the imaging window from t = 1 to 11 min after injecting TM2, the average apparent diffusion coefficient of DNA loci was calculated to be 1.6×10^{-4} μm^2 s^{-1}. This method allows us to visualize the change in average DNA mobility over the course of the experiment. For better comparison, previously obtained data for LL-37 and Cecropin A are plotted alongside (55). The black and pink horizontal dash lines in Fig. 2 represent, respectively, D_{app} values for normal growing cells and cells treated with CCCP and 2-deoxy-glucose (a combination that depletes ATP by dissipation of the proton motive force and prevention of glycolysis, which we term "CCCP treatment"). These data points were added to offer visual baseline controls.

TM1, TM4, TM8, TM9, TM10, TM11, TM15, and TM18 all decreased DNA loci motion below the level of ATP depletion within the first 25 min (Fig. 2), with TM5 and TM6 showing slower reactivity. During the observed experimental time frame following the addition of these two peptoids, only a fraction of the cells appeared permeabilized by phase contrast image and exhibited decreased motion of the DNA loci. TM3 and TM7 appeared to be ineffective, showing high MIC results (Table 1) and apparently failing to reduce DNA loci motion below ATP depletion levels even at much higher concentrations than the other peptoids tested (Fig. 2*D*). The initial drop of DNA loci motion observed for both TM3 and TM7 within the first 10-min time window can most likely be traced back to osmotic stress induced by the high peptoid concentrations used for injection (100 μM of TM3 and 400 μM of TM7). This is evidenced by the decrease in cell length and is consistent with the plasmolysis phenomenon we observed in a previous study upon flowing polycationic polymers (52). The resulting decrease in cytoplasmic volume might increase the molecular crowding effect, thereby impeding the diffusion of large chromosome loci (77, 78).

Most active peptoids, as identified by their low MIC values, generally exerted their effects within 25 min after injection as *Dapp* reached its final plateau value. To determine the final effect, we therefore calculated final MSD by combining the trajectories of the trials after 25 min of injection for each peptoid (Fig. 2 *E–H*). This 25-min time point was chosen as it also enables a direct and rigorous comparison of peptoid potency against antimicrobial agents we have previously characterized (52, 55).

MSD plots for normal growing cells show a clear negative curvature (Fig. 2 *E–H*), and plots for TM3 and TM7 seem to follow this trend. This is a signature of subdiffusive motion, as expected for the local dynamics of a small segment within a large, confined polymer (68, 74). The degree of curvature decreases for

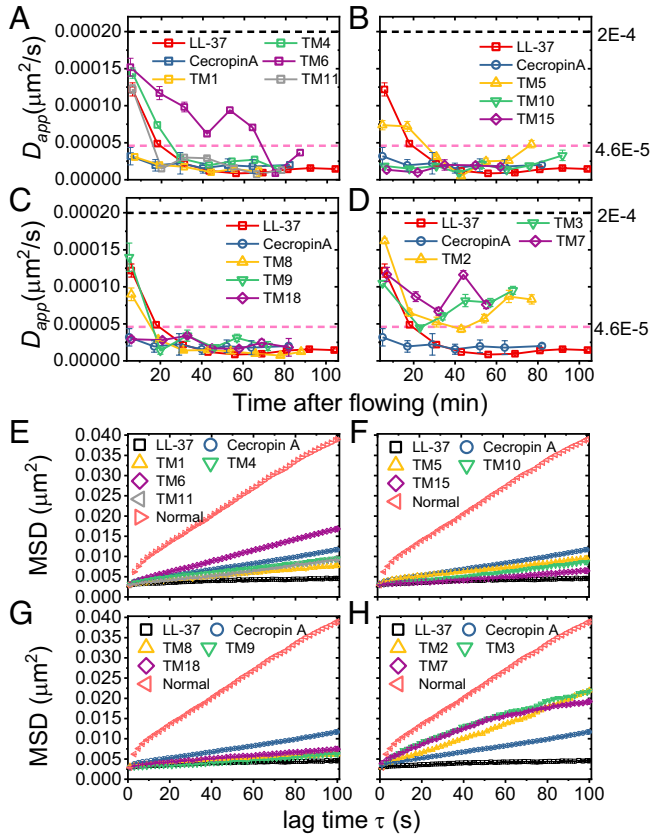

Fig. 2. DNA loci dynamics after exposure to peptoids. (*A–D*) Apparent diffusion coefficient D_{app} of DNA loci at different time points after adding peptoid at t = 0. Reference values of normal cells and ATP-depleting cells are displayed as black and purple dashed lines, respectively. Each time point represents the D_{app} averaged over all DNA trajectories in one field of view in a 10-min window, with images taken at 1 s/frame. The time point displayed represents the center of the 10-min window. The apparent diffusion coefficient D_{app} is obtained from a linear fitting of the first 10 points in the MSD plot. (*E–H*) MSD vs. lag time τ for DNA loci 25 min after exposure to different peptoids, obtained from movies taken at 1 s/camera frame for 600 frames. MSD covering 100 s; only half of the data are plotted for clarity. Experiments were performed in multiples, and SD are shown.

the less mobile DNA loci following administration of some peptoids. To enable semiquantitative comparisons on the 10 s timescale, an apparent diffusion coefficient (D_{app}) was computed for each MSD curve (Table 2), based on the linear fit using the first ten MSD points.

In addition to thermal motion, the motion of chromosomal loci is facilitated by ATP-dependent mechanical fluctuations (79). To mechanistically compare the efficacy of our peptoid series, we categorized them into three groups, based on the final extent to which they reduced the D_{app} of DNA loci. These classifications use two key benchmarks for comparison: the D_{app} of ATP depleted cells (representing the inhibition of nonthermal motion alone) and the D_{app} induced by LL-37 (representing complete chromosomal freezing, similar to chemical fixation). Based on these benchmarks, the peptoids were classified as: 1) Highly effective: This group, including TM1, TM4, TM8, TM9, TM10, TM11, TM15, and TM18 all rapidly rigidify DNA to a level comparable to LL-37 or cells fixed by formaldehyde, indicating a potent biophysical mechanism of action that goes beyond metabolic arrest. 2) Moderately effective: This group (TM2, TM5, and TM6) reduced DNA mobility, but less completely or more slowly than the first group. TM5 was the most active antimicrobial compound within this group, acting comparably to Cecropin A. However, the effect of TM5 is heterogenous on cell populations, resulting

Table 1. Minimum inhibitory concentration of peptoids against *E. coli*

Peptoid	RP-HPLC RT (min)*	MIC(μM)† VH1000 (WT)‡	JCW154‡	MDG196‡
TM1	3.68	6.25	6.25	6.25
TM2	3.84	25	50	25
TM3	3.59	100	100	100
TM4	4.02	12.5	12.5	12.5
TM5	3.36	12.5	12.5	12.5
TM6	3.39	12.5	12.5	12.5
TM7	3.08	>100	>100	>100
TM8	3.68	12.5	12.5	12.5
TM9	3.94	12.5	12.5	12.5
TM10	4.22	12.5	12.5	12.5
TM11	3.38	12.5	12.5	12.5
TM15	3.11	12.5	12.5	12.5
TM18	3.35	12.5	12.5	12.5
LL-37	–	4	4	4
Cecropin A	–	2	2	2

*retention time (min).
†minimum inhibitory concentration (μM).
‡*E. coli* strains details are presented in *SI Appendix*, Table S1.

in a mixture of permeabilized cells and a small fraction of intact cells (Fig. 3), which might explain why the overall diffusion coefficient of DNA loci did not reach the completely "frozen" state after administration of TM5. The effect of TM6 is similar to that of ATP-depleted cells. 3) Ineffective: As expected, TM3 and TM7 had no significant antimicrobial effect, and their D_{app} remained

Table 2. Mean diffusion coefficient of the DNA locus *Right2* and ribosome

Cell Treatment	D_{app} (μm²/s) (1 s/frame) for DNA loci after 25 min of injecting peptoid	D_{app} (μm²/s) (30 ms/frame) for ribosomes after 25 min of injecting peptoid
Normal growth*	$(2.0 \pm 0.2) \times 10^{-4}$	0.042 ± 0.001
CCCP+2-deoxyglucose*	$(4.6 \pm 0.2) \times 10^{-5}$	0.028 ± 0.001
LL-37†	$(1.0 \pm 0.1) \times 10^{-5}$	0.018 ± 0.001
Cecropin A†	$(3.1 \pm 0.4) \times 10^{-5}$	0.023 ± 0.001
Fixed cells*	$(7.6 \pm 2.1) \times 10^{-6}$	–
TM1	$(1.5 \pm 0.2) \times 10^{-5}$	0.015 ± 0.001
TM2	$(5.8 \pm 0.4) \times 10^{-5}$	0.034 ± 0.002
TM3	$(9.5 \pm 0.5) \times 10^{-5}$	–
TM4	$(1.8 \pm 0.3) \times 10^{-5}$	0.023 ± 0.001
TM5	$(2.6 \pm 0.2) \times 10^{-5}$	0.016 ± 0.001
TM6	$(4.8 \pm 0.3) \times 10^{-5}$	0.045 ± 0.002
TM7	$(8.6 \pm 0.5) \times 10^{-5}$	–
TM8	$(1.2 \pm 0.1) \times 10^{-5}$	0.011 ± 0.001
TM9	$(1.3 \pm 0.3) \times 10^{-5}$	0.013 ± 0.001
TM10	$(1.5 \pm 0.1) \times 10^{-5}$	–
TM11	$(1.6 \pm 0.2) \times 10^{-5}$	0.027 ± 0.001
TM15	$(1.1 \pm 0.2) \times 10^{-5}$	0.026 ± 0.001
TM18	$(2.0 \pm 0.2) \times 10^{-5}$	0.029 ± 0.002

*Data from Zhu et al. (55) included here for comparison.
†Data from Zhu et al. (52) included here for comparison.

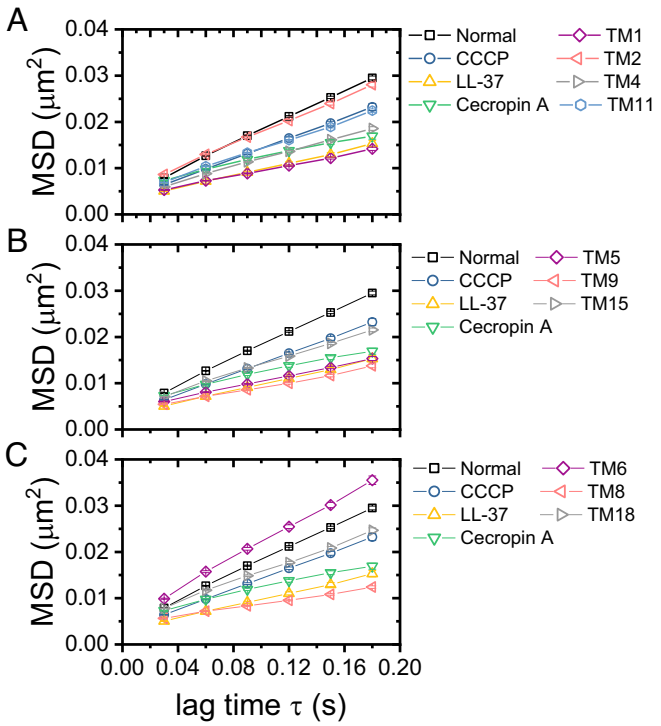

Fig. 3. Ribosome MSD vs. lag time from S2-mEos2 trajectories taken at 30 ms/frame in after exposure to the peptoids indicated in the legends of figure *A*–*C*. The apparent diffusion coefficient D_{app} is obtained by applying a linear fit to the first three data points (Table 2).

high, even above the ATP-depletion level, consistent with their high MIC values (Table 1).

Slowing of Ribosome Diffusion. We next assessed ribosome mobility to determine if these effects extended to other major intracellular components. We tracked ribosome diffusion before and after administration of the peptoids using Photoactivated Localization Microscopy (PALM) (63). Strain MSG196 was used in these experiments, as its chromosomal DNA is altered to append a photoconvertible mEos2 protein to the C-terminus of the ribosomal protein S2 (*SI Appendix*, Table S1) (80). We tracked 30S ribosomal subunits, which occur as either free 30S subunits or 30S subunits incorporated into translating 70S ribosomes, including 70S-polysomes (81, 82). The ribosome movies were acquired at 30 ms/frame. Only those trajectories that lasted six steps or longer were analyzed, and the longer trajectories were truncated at the sixth step to ensure uniform statistical weighting (*Materials and Methods*). In Fig. 3, MSD plots for ribosomes (S2-mEos2) are compared for the different cases. The apparent diffusion coefficient D_{app} was obtained by applying a linear fit to the first three data points (Table 2).

A similar pattern of activity as in DNA was observed, allowing us to classify the peptoids based on their impact on ribosome diffusion, again using ATP depletion and LL-37 as benchmarks. The most potent compounds (TM1, TM4, TM5, TM8, TM9) rigidified ribosome motion more than ATP depletion, reaching a frozen state comparable to that induced by LL-37. TM11, TM15, and TM18 reduced ribosome motion to a level similar to that of CCCP treatment (ATP depletion). Finally, the ineffective peptoids (TM2 and TM6) had no significant effects on ribosome dynamics.

Permeabilization of Cytoplasmic Membrane (CM). To detect membrane permeabilization by peptoids, 5 nM Sytox Orange was added to the solutions of peptoids prior to administration. This nucleic acid stain exhibits a dramatic increase in fluorescence upon accessing the cytoplasm and binding to the intracellular DNA, thus serving as a marker for membrane integrity loss. Phase contrast and fluorescence images were interleaved with an overall cycle time of 12 s/frame. In each cycle, images were collected using phase contrast (enabling measurement of tip-to-tip cell length as a function of time) and the fluorescence caused by Sytox Orange (55, 83). This allowed for the monitoring of cell growth and the onset of permeabilization of CMs by peptoids over a time period of 60 min. At time $t = 0$, a flow of 1× MIC of peptoids in warm, aerated EZRDM was initiated through a microfluidic chamber containing plated *E. coli* cells.

A typical result for a single cell after injecting TM15 is shown in Fig. 4*A*. Cell growth, as inferred from cell length vs. time, halted within 5 min after exposure to TM15 (Fig. 4*A*). Cell length then gradually shrunk as the peptoid gained access to the periplasmic space, consistent with our previous work on LL-37 (55) and synthetic polymers (52). We attribute this shrinkage to plasmolysis, driven by osmotic stress (84). High concentrations of the polycationic compounds and their counterions translocate across the outer membrane (OM) and accumulate in the periplasm. This rapid influx of solutes creates a significant osmotic upshift, which draws water out of the cytoplasm and causes it to shrink. At $t = 4$ min, the CM was permeabilized and Sytox Orange rapidly gained access to the cytoplasmic space as indicated by the gain in fluorescence signal. To calculate the fraction of CM permeabilization (CMP) as a function of time across the most active peptoids, the time needed for the increase in fluorescence intensity of Sytox Orange was directly translated as the time of CMP (Fig. 4*B*) (83). For the cases of active peptoids such as TM1, TM4, TM11, TM15, the Sytox Orange assay showed that essentially all cells had their CM permeabilized within 25 min of injection (Fig. 4*B*). This validated our choice of 25 min as an informative peptoid treatment time for calculating MSD. TM1 exhibited the highest efficiency and permeabilized almost all the cells within only 5 min. TM2 and TM5 achieved membrane permeabilization at a slower rate than TM1, TM4, TM11, and TM15, with a fraction of cells remaining intact, even 40 min after contact with TM2 or TM5.

Differences in Physical Effects of Treatment with TM1 and TM5 on *E. coli* Bacteria. Soft X-ray tomography was utilized to compare the physical effects of TM1 and TM5 on *E. coli* as shown by the large difference in membrane permeabilization rates, as compared with an untreated *E. coli* cell. The cells were treated with 1× MIC at 37 °C for 4 h. As seen from Fig. 5, *E. coli* treated with TM5 appeared highly altered, with damage to one cell pole, plus differences in cytoplasmic mass distribution; distinct from what is seen for TM1, where the membrane structure is profoundly damaged near the center of the cell. For both TM1- and TM5-treated bacterial cells, profound changes in the spatial distribution of the intracellular biomass—very different from the healthy control cell's internal structure—are apparent, and since these cells were treated for 4 h, we also know that this biomass has lost its normal dynamic mobility and is either fully "frozen" (TM1), or close to frozen (TM5).

TM1 Binding and Complexation with Nucleic Acids. We showed above that TM1 permeabilizes the CM within 5 min of injection (Fig. 4*B*), even faster than LL-37, and rigidifies DNA and reduces ribosome motions as effectively as LL-37. We examined the differences between DNA/RNA binding ability and structural and biophysical properties of the TM1-DNA/RNA complexes that were formed. Circular dichroism was used to characterize the structural changes and interactions between TM1 and different types of

ssDNA and ssRNA, since cationic charges in the amphiphilic peptoids electrostatically interact with the negative charges of the phosphate groups in DNA/RNA. The sequences of the DNA and RNA used in this study are shown in *SI Appendix*, Table S2. As seen in *SI Appendix*, Fig. S2, significant changes in the CD spectrum were observed for oligonucleotides containing adenine, in the case of both DNA and RNA. The melting temperature (T_m), (included in *SI Appendix*, Table S4) defined as the temperature where 50% of the complexes have been dissociated, provides evidence of the stability of the peptoid–DNA or DNA–DNA duplexes (85). In fluorescent polarization assays, the peptoid bound single-stranded RNA (rA12 and rU12) and single-stranded DNA (A12 and T12) with a binding constant (K_D) of 0.41, 0.45, 0.77, and 0.82 μM, respectively (Table 3 and *SI Appendix*, Fig. S4).

To visualize the structures of the peptoid-DNA/RNA complexes, TEM with negative staining was used. Aggregates were found to be polydisperse with a diameter of 2 nm to 2 μm (*SI Appendix*, Figs. S6 and S7), in good agreement with the sizes determined by dynamic light scattering (DLS) (*SI Appendix*, Figs. S8–S10).

Discussion

There is a growing recognition of how the dynamic mechanisms of action of antimicrobial peptides (AMPs) are more complex than solely membrane disruption (43, 55, 86). However, whether this also fully extended to AMP-mimetic peptoids in their dynamics had yet to be determined. In a previously presented study, we showed how both antimicrobial peptides and peptoids cause the aggregation of intracellular biomacromolecules, including ribosomes within the *E. coli* cytoplasm, using transmission electron microscopy and soft X-ray tomography (46). In the results presented here, we provide further proof of intracellular mechanisms of action for antimicrobial peptoids using live-cell imaging, which also gives us information on the dynamics of their mechanisms. The results reveal how all active antimicrobial peptoids decrease the diffusive motion of several key cytoplasmic components including DNA and ribosomes after entering the cell. The effect is similar to what has been reported for the human peptide LL-37 (55). However, several of the active peptoids (TM1, TM8, TM9, TM10, TM11, TM15, TM18) act even faster on the DNA loci dynamics than LL-37 itself (Fig. 2). When comparing the diffusion coefficient of the DNA locus *Right2* (Table 2) after flowing the peptoids and the control peptides,

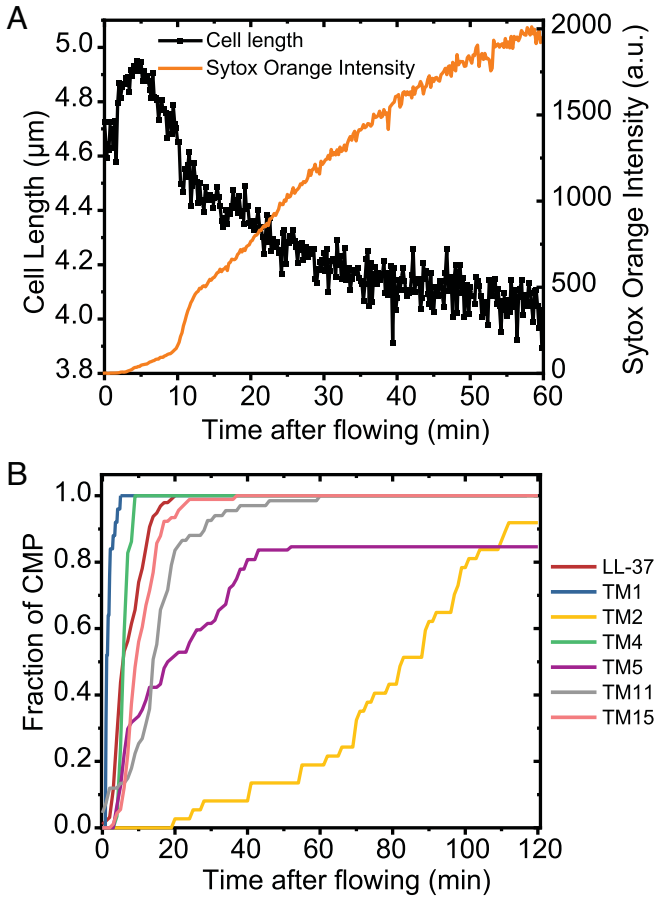

Fig. 4. (*A*) Cell length (black) and Sytox Orange (orange) fluorescence intensity vs. time for a single cell after injection of 1× MIC peptoid TM15 at $t = 0$. A cell was defined as "permeabilized" at the first time point (frame) where its Sytox Orange intensity rose above mean fluorescence background. (*B*) Fraction of Cytoplasmic membrane permeabilization by several peptoids and LL-37 (LL-37 data taken from ref. 55). The curve indicates the percentage of cells with permeabilized CM as judged by the onset of Sytox Orange fluorescence.

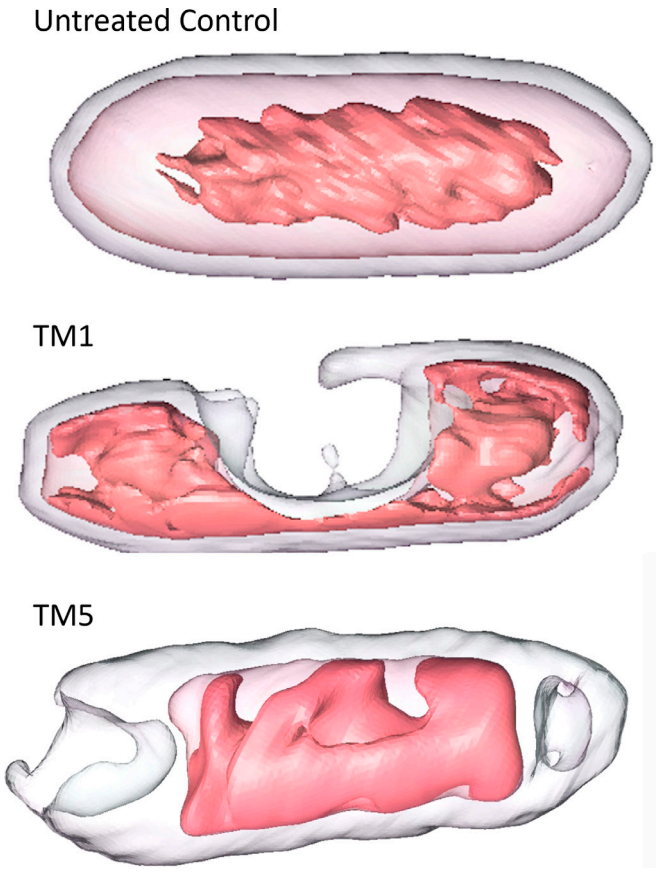

Fig. 5. Soft X-ray tomography comparing untreated *E. coli* bacteria with addition of 1× MIC of TM1 and TM5.

Table 3. Binding affinities and specificities of TM1 as determined by the binding constant (K_D)

	K_D (μM)
A_{12}-TM1 pair	0.77
T_{12}-TM1 pair	0.82
rU_{12}-TM1 pair	0.45
rA_{12}-TM1 pair	0.41
A_{24}-TM1 pair	0.25
T_{24}-TM1 pair	0.26
plasmid DNA-TM1 pairs	0.00002

LL-37 and Cecropin A, we find that the effects are in a comparable range, except for peptoids TM3 and TM7, which were found to be wholly inactive, as confirmed by their high MIC values (Table 1). The ability of peptoids to slow down ribosome motion is, in general, similar to their effects on DNA loci, but with some informative exceptions. The most potent peptoids including TM1, TM4, TM5, TM8, and TM9, were able to reduce ribosome motion exceeding that of ATP depletion and reach a frozen state comparable to, or even more profound, than that induced by LL-37 (55). This extreme rigidification cannot be explained by metabolic depletion alone and provides strong evidence for a direct physical interaction, likely physical crosslinking. We propose that upon flooding the cytoplasm, these peptoids engage in electrostatic binding with anionic components of the ribosome, leading to their immobilization (55). These peptoids comprise both cationic, lysine-like side chains that can bind electrostatically to the phosphates in the nucleic acid backbones of DNA and ribosomes, and phenyl-group containing *N*spe side chains that can interact with DNA and RNA bases via aromatic interactions (either stacking, or edge-to-face). In contrast, the ineffective peptoids TM2 and TM6 did not show any noticeable effects in reducing ribosome dynamics. Intriguingly, TM11, TM15, and TM18, which belong to the most active group of peptoids in terms of rigidifying DNA, only slowed down ribosome motion, similar to CCCP treatment, suggesting that the effect is primarily a consequence of ATP depletion. This indicates that while the mechanism(s) of binding and rigidifying ribosomes and DNA among these different peptoids are likely similar given their related physicochemical structures, they are not identical: small molecular differences can alter binding preferences and kinetics for different intracellular targets. The differences in the activity cannot be explained solely by the net charges of the peptoids, as TM6 (inactive) has a higher net positive charge (+5) than for example active compounds TM8 and TM9 (+3) (Fig. 1), but TM8 and TM9 are both much better at rigidifying DNA and reducing ribosome motion, demonstrating that high charge alone is insufficient for activity. Similarly, the hydrophobicity of the peptoids alone cannot explain the differences in activity. As an example, TM2 is more hydrophobic than TM1 and TM8 (Table 1), but both TM1 and TM8 are superior in terms of activity as seen by the presented assays. Rank et al. found that the effect of AMP mimicking copolymers was dependent on other factors like subtle variations in conformational behavior (54), similar to what was observed here. However, in our case the self-association properties may also play a role as suggested by Nielsen et al. (25). Indeed, the MIC data for the TM peptoid library presented here against *E. coli* supports the positive correlation between antimicrobial activity and ability to self-assemble as presented against all ESKAPE pathogens in Nielsen et al. (25), including the lack of activity for the non-self-assembling TM7 peptoid. In all, a complex interplay of charge, charge density, hydrophobicity, and self-association properties dictates overall antimicrobial effect.

A key observation from our single-cell, real-time fluorescent imaging study is the rapid timescale of DNA rigidification, with the most potent peptoids inducing maximal effects within 25 min. This timeframe is crucial for understanding the mechanism of action. Our previous work established a direct temporal link between rigidification of DNA and ribosome and various other catastrophic events such as cytoplasmic membrane permeabilization and coacervation (52, 55). For instance, Zhu et al. revealed that for LL-37, the "freezing" of DNA loci occurs simultaneously with the permeabilization of the cytoplasmic membrane (55). Furthermore, recovery experiments in that study demonstrated that this lethal process is irreversible even if flowing fresh medium for 80 min after exposure to LL-37 for 20 min (55). The rapid kinetics observed for the peptoids in this study are highly consistent with this established model.

Moreover, active peptoids freeze DNA and ribosome motion more profoundly than ATP depletion alone (79). These results confirm that DNA rigidification is not a downstream consequence of metabolism depletion but rather a primary event within the lethal cascade. This reinforces the conclusion that while membrane permeabilization is the gateway for entry, the subsequent and rapid crosslinking and rigidification of intracellular targets like the chromosome is a critical determinant of overall antimicrobial potency (52, 55).

When looking in more detail into the ability of the peptoids to permeabilize the bacterial membrane, TM1, TM4, TM11, TM15 were found to be able to permeabilize the membrane of *E. coli* within 5 to 25 min. Interestingly, the permeabilization rates of TM1 and TM4 are faster than what has been reported for LL-37 (55). While this connects well with TM1 showing a faster effect on DNA loci than LL-37, TM4 displays a rate of effect on DNA loci similar to LL-37 and is also quite active.

For TM2 and TM5, the permeabilization rate is significantly slower than for the other peptoids, with observations of intact cells even after 40 min. Interestingly, TM2 does indeed show slightly higher MIC values compared to the other peptoids, while TM5 shows similar activity as the other peptoids. As seen from Fig. 5, TM5 seems to have a different physical effect on the bacterial cell than TM1, which may explain why these peptoids are both active antimicrobials, but display very different membrane permeabilization rates. This also indicates that the rate of permeabilization alone does not necessarily dictate the antimicrobial activity. The high potency of TM5 despite a relatively slow rate of membrane permeabilization provides evidence that the lethal event for this class of compounds may be the catastrophic shutdown of intracellular processes following entry into the cytoplasm, underscoring the importance of intracellular targets.

Similar results (minus the dynamics) were observed in Chongsiriwatana et al. (46). With these results in hand, we suggest that the true correlation is between antibacterial activity and the combined ability of a given peptoid/peptide to cross the bacterial membrane (and in some cases, to disrupt it) and to interact with intracellular targets, such as DNA and ribosomes. For example, LL-37 has recently been shown by Nielsen et al. to also have a significant effect on lipid dynamics even at very low concentrations, and a detergent-like membrane disruptive effect when increasing the concentration (87). It is likely that at least several of the peptoids presented here also will have membrane disruptive properties similar to that of LL-37 due to the physicochemical similarities. This should be considered, together with the intracellular effects reported in this work, to explain the high antimicrobial activity that these peptoids display.

The large difference in kinetics of membrane permeabilization of TM1 and TM2 (<5 min vs. ~40 min, respectively), is of particular interest, as TM2 is a 6-mer analogue of TM1, partly halogenated with two bromines (Fig. 1). This could potentially be explained by the addition of bromines strengthening the hydrophobic interactions with the acyl lipid tails in the bacterial membrane. However, TM4, which is similar to TM2 but consists of four brominated *N*spe groups (Fig. 1), shows significantly faster permeabilization and stronger effect in inhibiting the motion of DNA and ribosome. We have previously shown that halogen substitution in peptoids increases the antimicrobial activity of short peptoids (38). The presented data revealed that degree of halogen

substitution significantly affected the physicochemical properties as well as the antimicrobial efficacy of peptoids. This supports the large difference in membrane permeabilization and rigidification of DNA and ribosome here observed between TM2 (two bromines) and TM4 (four bromines). The other slower acting peptoid TM5 does not include halogens, but has an alkyl tail, promoting self-assembly into similarly shaped ellipsoidal micelles in aqueous solution. The design of TM15, with the same structure as TM5 but with the addition of one extra charged *N*Lys group, results in a faster membrane permeabilization.

Analyses of binding of TM1 to single-stranded DNA, RNA, and double-stranded DNA provide support for a mechanism of action involving intracellular aggregation of biomolecules. The CD studies showed that the net change in CD spectra was greatest for A_{24} and rA_{12} (*SI Appendix*, Fig. S2). Using UV spectroscopy, the T_m of A_{12}- peptoid pairs was found to be slightly higher than the T_m value of T_{12}- peptoid pairs under identical conditions (*SI Appendix*, Table S4). Fluorescence polarization experiments showed that the fluorescence polarization value of the peptoid increased as a function of DNA/RNA concentration (*SI Appendix*, Fig. S4). Additionally, the K_D value obtained for A_{12} is slightly lower than that of T_{12}, suggesting a higher binding affinity (Table 3). This result is similar to the binding trend suggested by T_m analysis. Taken together, it was found that binding affinity is dependent on nucleic acid length and, based on K_D values, that the peptoid has a much higher affinity for ssRNA (rA_{12} and rU_{12}) than ssDNA (A_{12} and T_{12}). This demonstrated interaction with both DNA and RNA further supports the theory that TM1 acts through a mechanism involving intracellular aggregation of biomolecules. The higher affinity to RNA compared to DNA suggests that in vivo it may preferentially bind to the bacterial ribosomes (RNA). This is consistent with the slightly improved effect of TM1 on slowing motion of ribosomes as compared to DNA loci as discussed above.

In summary, the results presented here further support the hypothesis that antimicrobial peptoids can act on intracellular targets within the bacterial cell, similar to AMPs including LL-37 and Cecropin A (55). The mechanism of action of TM1 and some of its shorter alkylated and brominated analogues involve rapid membrane permeabilization followed by intracellular aggregation of biomolecules. We have shown that some peptoids permeabilize the CM even faster than LL-37—and rigidify DNA and ribosomes just as effectively.

Overall, we conclude that for all peptoids presented and discussed here, strong interactions with intracellular targets, including both ribosomes and nucleic acids, seem to be an important key to understanding the mechanism. However, as seen from the tomography image of TM5-treated *E. coli* and the lack of direct correlation between permeabilization and activity, the intracellular mechanism is likely accompanied by significant membrane disruption. Taken together, our results demonstrate that potent antimicrobial activity is a multiparameter optimization problem requiring a balance of properties to 1) efficiently cross bacterial membranes and 2) effectively bind intracellular targets. The bacterial cytoplasm comprises a high concentration of polyanionic biopolymers (e.g., chromosome, ribosome, and RNA), which contribute ~2×10^8 (~200 mM) negative charges, primarily compensated by K^+ under our growth conditions (88, 89). This preponderance of polyanionic biopolymers provides electrostatic lubrication to facilitate diffusion during normal growth (90). However, it also makes bacteria highly susceptible to extensive binding and adsorption of polycationic agents, once these agents penetrate the membranes. Our previous quantitative measurements on LL-37 provide a precedent for this mechanism (55). We found that an external concentration of 20 μM LL-37 can lead to an internal concentration of 90 mM, a massive >1,000-fold accumulation. Theoretical estimation using the McGhee-von Hippel model generates similar results (55, 91). Driven by similar interactions, we propose that the active peptoids in this study displace the native counterions and form strong, noncovalent, multivalent electrostatic bonds with the intracellular polyanions. This action forms a dense network of pseudo-crosslinks in the cytoplasm, transforming the dynamic bacterial cytoplasm into a rigid, gel-like state. This cytoplasmic rigidification appears to be a general mechanism for a broad class of polycationic antimicrobials, including antimicrobial peptides LL-37 (55), synthetic polymers (52), and peptoids in this study, providing a powerful, resistance-evading strategy for killing bacteria. While it is difficult to attribute cell death to a single event, this global freezing of the intracellular environment following an influx of peptoid-derived positive charges represents a catastrophic state from which bacteria are unlikely to recover. Crucially, because this mechanism targets the general physical properties of the cytoplasm rather than a specific protein, it is unlikely to be circumvented by common resistance pathways, such as single-point mutations. Peptoids displaying more than one mode of action could be highly beneficial in limiting peptoid resistance development by the bacteria and may explain why no change in MIC of TM5 was observed after 30 successive exposures of *P. aeruginosa* to sub-MIC in a recent study (26), making the peptoids a promising therapeutic against multiresistant bacterial strains.

Materials and Methods

Synthesis of TM Peptoids. All reagents for peptoid synthesis were purchased from Applied Biosystems (Foster City, CA) and Sigma-Aldrich (Milwaukee, WI). Resin, Fmoc-protected amino acids, and 5(6)-carboxyfluorescein were purchased from Novabiochem (San Diego, CA). Unless otherwise stated, all solvents were purchased from Fisher Scientific (Pittsburgh, PA). Peptoids were synthesized manually on Rink amide resin according to the submonomer method (20). After synthesis, oligomers were cleaved and deprotected in trifluoroacetic acid (TFA)/triisopropylsilane/water for 30 min. Product purity was determined by means of analytical UPLC/MS and purification by preparative HPLC. After purification, peptoids were lyophilized and ion exchange from TFA to HCl salt was performed. For more details, see the *SI Appendix*.

Cell Growth and Preparation for Imaging. Bulk cultures were grown in an EZ rich, defined medium (EZRDM), which is a 3-(N-morpholino)propanesulfonic acid (MOPS)-buffered solution at pH = 7.4 supplemented with metal ions (M2130; Teknova), glucose (2 mg/mL), amino acids and vitamins (M2104; Teknova), nitrogenous bases (M2103; Teknova), 1.32 mM K_2HPO_4, and 76 mM NaCl. Cultures were grown from glycerol frozen stock to stationary phase overnight at 30 °C. Subcultures were grown to exponential phase (OD = 0.2 to 0.6 at 600 nm) at 30 °C before sampling for microscopy experiments (51, 67, 92).

Strains used in the study and the corresponding MIC are summarized in Table 1 and *SI Appendix*, Table S1. Strains that express labeled species from a plasmid were grown with the addition of 100 μg/mL ampicillin.

For studying cells under ATP-depleting conditions, cells were treated with 200 μM carbonylcyanide-*m*-chlorophenylhydrazone (CCCP) and 1 mM 2-deoxyglucose (73, 79, 93–96). These ingredients were added to the subcultures for 10 min prior to imaging. During the imaging, EZRDM was supplemented with each drug at the same concentration (55).

Two different imaging methodologies were employed: a flow chamber and a static chamber. Single-cell, time-lapse imaging experiments on the DNA locus *Right2* were carried out at 30 °C in a PDMS-based microfluidics chamber consisting of a single rectilinear channel of uniform height of 150 μm, width of 6 mm and length of 11 mm. The total chamber volume is ~10 μL. After attachment of the PDMS chamber to the glass coverslip, 10 μL of 0.01% poly-L-lysine (molecular weight >150,000 Da) was flowed through the chamber and

allowed to adsorb for 30 min. The chamber was then rinsed thoroughly with ultrapure water to remove excess poly-L-lysine. When the subcultures had grown to midlog phase, a culture containing *E. coli* cells was flowed through the microfluidic chamber, followed by fresh, aerated, warmed EZRDM to wash away any unbound cells. The remaining cells were immobilized on the coverslip but grew normally, as illustrated in refs. 51 and 82. The PDMS ceiling of the microfluidics device is permeable to the ambient gases N_2 and O_2. The microfluidics chamber allows the throughflow during imaging of appropriate chemicals necessary for the experiment, such as peptoid solutions or Sytox Orange (S11368, ThermoFisher Scientific) (92).

Single-molecule imaging of ribosomes (S2-mEos2) was carried out in a static chamber. First, ~150 μL of cell culture was placed within a CoverWell perfusion chamber gasket (Invitrogen) on a poly-L-lysine-coated, cleaned coverslip to fill the entire chamber volume. After waiting 2 min for the cells to adhere to the coverslip, plated cells were rinsed with appropriate fresh, warmed, aerated media to wash away any nonadhered cells. For imaging of cells under normal growth conditions, EZRDM was used as rinsing medium. Cells were allowed to grow normally for at least 30 min under these conditions. For peptoid-treated conditions, the rinsing medium was peptoid in EZRDM solution. The cells were maintained at 30 °C throughout the imaging process using an automatic temperature controller (52).

Microscopy. All imaging was performed on a Nikon Eclipse Ti inverted microscope (Nikon) with either an oil immersion 100×, 1.3 NA phase contrast objective or an oil immersion 100×, 1.45 NA phase contrast objective (CFI Plan Apo Lambda DM; Nikon Instrument). The images were further magnified 1.5× unless otherwise specified. Fast shutters (Uniblitz LS2; Vincent Associates) were used to synchronize illumination and image acquisition. Images were recorded by a backilluminated EMCCD camera with 16 μm × 16 μm pixels (either Andor iXon DV-897 or Andor iXon DV-887; Andor Technology). Each pixel corresponds to 105 × 105 nm^2 of the sample with an overall magnification of 150× (92).

Studies of the motion of DNA loci *Right2* labeled by ParB-GFP (strain JCW154) were carried out in the flow chamber (96, 97). Specifically, live *E. coli* cells were immobilized on a poly-lysine coated coverslip in a microfluidic channel that enabled us to begin flowing the antimicrobial agent at known concentration at time $t = 0$ and image the cell at different time points after contact with the peptoids (76). ParB-GFP loci were imaged using 488 nm excitation (Coherent Sapphire laser), expanded to illuminate the field of view uniformly. The laser intensity was ~100 W/cm^2 at the sample plane. The emission filter was HQ525/50 (Chroma Technology). The loci were tracked with good signal-to-noise ratio for 600 frames at 1 s/frame and 50 ms exposure time (a time duration of 10 min) with a localization precision of ~35 nm. Images of the DNA stain Sytox Orange were collected at 12 s/frame using a 561 nm laser with a power density ~2.5 W/cm^2. A HQ600/50 M filter (Chroma Technology) was used. For superresolution imaging of ribosomes labeled with S2-mEos2 (strain MDG196), the fluorescent protein was photoconverted using a 405 nm laser at ~4 to 12 W/cm^2 and subsequently imaged using a 561 nm excitation laser at ~2 kW/cm^2. The emission filter used was an ET610/75 (Chroma Technology). Ribosome S2-mEos2 was imaged at a frame rate of 31.2 Hz, with an exposure time of 30 ms (92).

Data Analysis. Images were analyzed using a MATLAB graphical user interface developed in the Weisshaar lab (83, 98). Images were smoothed and filtered to obtain a zero-based image. Bright spots were located with pixel-level accuracy using a peak finding algorithm that detects the local intensity maxima within an image. A user defined intensity threshold was applied as the minimum brightness of a pixel arising from a single molecule. The threshold range was carefully set to not reject a real single molecule in the raw images or to include background noise (55, 92).

A modified MATLAB version of the tracking program written by Crocker and Grier (99) was used. As described before (51, 55, 67, 82, 100, 101), a centroid algorithm was used to locate the identified particles with subpixel resolution. Centroids of the bright spots were calculated from a 7 × 7 pixel square containing the entire bright spot, centered on the local maximum determined by the peak finding algorithm. The centroid positions from successive frames were connected to form a trajectory (92).

The time-averaged mean-square displacement (MSD) for a single trajectory with N steps is calculated as (68):

$$\begin{aligned} MSD(\tau) &= \left\langle \left(\vec{R}(t+\tau)-\vec{R}(t)\right)^2 \right\rangle \\ &= \frac{1}{(N-n)} \sum_{k=1}^{N-n} \left[\vec{R}_i\left(k\Delta t+\tau\right)-\vec{R}_i\left(k\Delta t\right)\right]^2 \\ &= \frac{1}{(N-n)} \sum_{k=1}^{N-n} \left[\vec{R}_i\left(k\Delta t+n\Delta t\right)-\vec{R}_i\left(k\Delta t\right)\right]^2. \end{aligned} \quad [1]$$

In our experimental conditions, the time-ensemble-averaged mean-square displacement over many trajectories was calculated as

$$\begin{aligned} MSD(\tau) &= \left\langle \left(\vec{R}(t+\tau)-\vec{R}(t)\right)^2 \right\rangle \\ &= \frac{1}{M} \sum_i \frac{1}{(N-n)} \sum_{k=1}^{N-n} \left[\vec{R}_i\left(k\Delta t+\tau\right)-\vec{R}_i\left(k\Delta t\right)\right]^2. \end{aligned} \quad [2]$$

Here, M is the number of trajectories over which the ensemble average is taken. The index k runs from 1 to a specific value given the lag time τ, providing the time average of each trajectory. The final MSD is an average over the ensemble and over time (74). For DNA loci imaged with 1 s/frame, k runs from 1 to 99. We used a linear fit of the first 10 points on the MSD plots to calculate the approximate apparent diffusion coefficients (55). For ribosomal S2-mEos2, k runs from 1 to 6, and we used a linear fit of the first three points on the MSD plots to calculate an approximate apparent diffusion coefficient via an average over thousands of trajectories (102).

The number of points used for the linear fit of the MSD curve was chosen to obtain an unbiased estimate of the diffusion coefficient (68). This choice involves a trade-off between minimizing the effect of localization error (which dominates at short time lags) and effect of poor statistical averaging (which dominate at long time lags) (103). Our approach was guided by the quantitative framework proposed by Michalet (102), which uses the reduced localization error $x = \frac{\sigma^2}{D\Delta t}$, to determine the optimal fitting range. The choice also ensures direct comparison with our previous work on LL-37 (55).

To account for the fact that fast-diffusing ribosomes are more likely to move out-of-focus and result in shorter trajectories, we standardized our analysis to ensure uniform statistical weighting and to avoid bias from overrepresenting slower particles. All trajectories lasting six steps or longer were analyzed, with trajectories longer than this being truncated at the sixth step before the MSD calculation. This standard procedure was applied consistently across all experimental conditions to ensure that comparisons of D_{app} between them are unbiased. If it is assumed that the least-squares, best fit to the first ten or three experimental points of a mean-square displacement plot is given by the equation MSD (τ) = $a + b\tau$, with b the slope and a the extrapolated intercept at lag time $\tau = 0$, then Michalet (102) has shown that the most accurate mean diffusion coefficient is given by $D = b/4$, and the best estimate of the dynamic localization error is $\sigma = 1/2\,(a + 4Dt_E/3)^{1/2}$, where t_E is the exposure time per camera frame. All MSD curves were generated by averaging the trajectories from all cells within the field of view to provide a quantitative measure of the overall efficacy of each peptoid (92).

Minimal Inhibitory Concentration (MIC) Determination against *E. coli* (ATCC 35218) Used for Soft X-Ray Tomography. MICs were determined in a 96-well microtiter plate. 75 μL of bacterial inoculum (1 × 10^6 CFU/mL) in Mueller-Hinton broth (MHB) was added to 75 μL of peptoid solution in MHB (prepared in serial dilution). Positive controls contained 75 μL of inoculum and 75 μL of MHB without peptoid. The MIC was defined as the lowest concentration of peptoid that inhibited 90% of bacterial growth after incubation at 37 °C for 18 h. MIC values reported were reproducible between three independent experimental replicates.

Soft X-Ray Tomography. For soft X-ray tomography cells (OD_{600} 0.6) were treated with 1× MIC at 37 °C for 4 h. X-ray datasets were collected using the XM-2 soft X-ray microscope operated by the National Center for X-ray Tomography at the Advanced Light Source of Lawrence Berkeley National Laboratory (LBNL). XM-2 is equipped with Fresnel zone plate-based condenser and objective lenses (made by the Center for X-ray Optics, LBNL) and is specifically designed to investigate biological samples at cryogenic temperatures. For soft X-ray tomography, cells

were washed five times with PBS and then rapidly transferred to thin-walled glass capillaries, and immediately flash frozen in a cryogenic gas stream (104). No additional staining procedures were used. Imaging was performed with the specimens under liquid nitrogen cooled helium gas atmosphere at all times. For each dataset, 90 projection images were collected sequentially around a rotation axis in 2° increments to give a total rotation of 180°; the microscope was equipped with a resolution defining 50 nm objective lens. An exposure time of between 150 and 300 ms was used (depending on synchrotron ring current). Manual alignment of images, based on fiducial markers, was performed using the IMOD package (105). Tomographic reconstructions were calculated using Amira software package (Mercury Computer Systems).

Calculation of Linear Absorption Coefficient (LAC) and Manual Segmentation. Reconstructed cells were segmented into subvolumes with similar LACs. The LAC for each voxel was measured directly from the experimental data. The absorption of soft X-rays follows Beer's Law, and therefore, is concentration and molecular species dependent. The LAC for a segmented organelle is a measure of the overall biochemical composition. Manual segmentation, measurements of voxel values to calculate LACs, and recording of movies were all carried out using the Amira software package (Mercury Computer Systems).

DNA/RNA Synthesis. Synthetic single-strand oligonucleotides were purchased from Integrated DNA Technologies (Coralville, IA) and used after HPLC purification. Plasmid DNA ($pGFP_{uv}$) was purchased from Clontech (Mountain View, CA). All DNA/RNA samples were dissolved in distilled pure water (RNA-free) for further experiments. Nucleic acids used in this study are shown in *SI Appendix*, Table S2.

Synthesis of TM1 Labeled with 5(6)-Carboxyfluorescein. TM1 was synthesized using a submonomer coupling method utilizing an Applied Biosystems 433A robotic peptide synthesizer with customized software protocols. For labeling at the N terminus, resin-bound TM1, 5(6)-carboxyfluorescein, DIC, and HOBt in DMF were incubated at room temperature for 1 h in the dark with mild stirring, as reported previously (106). The fluorescently labeled TM1 was cleaved from the resin with TFA/triisopropylsilane/water for 5 min in the dark with mild agitation. After filtering and washing the resin with water/acetonitrile, the labeled TM1 was analyzed by LC–MS then purified by preparative HPLC. For more details, see the *SI Appendix*.

Fluorescence Polarization Assay. DNA/RNA and approximately 100 nM fluorescein-labeled TM1 were mixed in 500 μL PBS (pH 7.2) at room temperature for 30 min. The fluorescence polarization values of samples were measured on a Beacon 2000 fluorescence spectrometer (Invitrogen, Carlsbad, CA), as described previously (107, 108).

Data, Materials, and Software Availability. The code for image analysis is available on GitHub (https://github.com/zhuyanyu123/peptoid-PNAS-paper-code) (83). Study data are included in the article and/or *SI Appendix*.

ACKNOWLEDGMENTS. J.E.N., K.S., J.S.L., and A.E.B. acknowledge funding from the US Public Health Services' NIH (including an NIH Pioneer Award to Annelise Barron, NIH/NIA grant # 1DP1 OD029517-01). A.E.B. also acknowledges funding from the Lifespan Research Institute, Stanford University's Discovery Innovation Fund, the Cisco University Research Program Fund, and especially, Dr. James J. Truchard and the Truchard Foundation. N.M. and H.J. were funded by the Danish Council for Independent Research, Technology and Production (Project no. 4005-00029). Y.Z., M.M., and J.C.W. acknowledge funding by the NIH (grants R01-GM094510). We gratefully acknowledge Dr. Jong Pil Park and Dr. Yoriel Marcano for their contributions to the DNA/RNA peptoid binding study. We gratefully acknowledge Dr. Michael Connolly and Dr. Behzad Rad at the Molecular Foundry for assistance with peptoid synthesis and sample preparation equipment. Work at the Molecular Foundry was supported by the Office of Science, Office of Basic Energy Sciences, of the US Department of Energy under Contract No. DE-AC02-05CH11231. The soft X-ray tomography and SAXS experiments were conducted at the Advanced Light Source (ALS), a national user facility operated by Lawrence Berkeley National Laboratory on behalf of the Department of Energy, Office of Basic Energy Sciences, through the Integrated Diffraction Analysis Technologies program, supported by the DOE Office of Biological and Environmental Research. The National Center for X-ray Tomography is supported by NIH NIGMS (P41GM103445), and SAXS beamline SIBYLS has additional support from the NIH project ALS-ENABLE (P30 GM124169) and a High-End Instrumentation Grant S10OD018483. We thank Dr. Jian-Hua Chen and Dr. Gerry McDermott for support with the X-ray Tomography experiments and Dr. Gregory Hura and Kathryn Burnett for support during the SAXS experiment, and Dr. Reidar Lund at the University of Oslo for valuable discussions regarding analysis of SAXS data.

Author affiliations: [a]Department of Chemistry, University of Wisconsin–Madison, Madison, WI 53706; [b]Department of Bioengineering, Schools of Medicine and of Engineering, Stanford University, Stanford, CA 94305; [c]Department of Science and Environment, Roskilde University, Roskilde 4000, Denmark; [d]The Molecular Foundry, Lawrence Berkeley National Laboratory, Berkeley, CA 94720; [e]Institute of Biological and Chemical Systems–Functional Molecular Systems, Karlsruhe Institute of Technology, Karlsruhe 76131, Germany; and [f]Institute of Functional Interfaces, Karlsruhe Institute of Technology, Karlsruhe 76131, Germany

Author contributions: Y.Z., J.E.N., N.M., S.B., U.S., J.C.W., H.J., and A.E.B. designed research; Y.Z., J.E.N., M.M., and B.F. performed research; N.M., C.H., and K.S. contributed new reagents/analytic tools; Y.Z., J.E.N., B.F., and J.C.W. analyzed data; and Y.Z., J.E.N., N.M., C.Z., J.S.L., and A.E.B. wrote the paper.

1. WHO, Critically important antimicrobials for human medicine, 6th revision (World Health Organization, Geneva, 2019).
2. M. S. Mulani, E. E. Kamble, S. N. Kumkar, M. S. Tawre, K. R. Pardesi, Emerging strategies to combat ESKAPE pathogens in the era of antimicrobial resistance: A review. *Front. Microbiol.* **10**, 539 (2019).
3. M. Zasloff, Antimicrobial peptides of multicellular organisms. *Nature* **415**, 389–395 (2002).
4. J. S. H. B. Koo, Antimicrobial peptides under clinical investigation. *Pept. Sci.* **111**, e24122 (2019).
5. M. Mahlapuu, J. Hakansson, L. Ringstad, C. Bjorn, Antimicrobial peptides: An emerging category of therapeutic agents. *Front. Cell. Infect. Microbiol.* **6**, 194 (2016).
6. J. A. Patch, A. E. Barron, Helical peptoid mimics of magainin-2 amide. *J. Am. Chem. Soc.* **125**, 12092–12093 (2003).
7. A. E. Barron, R. N. Zuckermann, Bioinspired polymeric materials: In-between proteins and plastics. *Curr. Opin. Chem. Biol.* **3**, 681–687 (1999).
8. C. W. Wu, T. J. Sanborn, R. N. Zuckermann, A. E. Barron, Peptoid oligomers with alpha-chiral, aromatic side chains: Effects of chain length on secondary structure. *J. Am. Chem. Soc.* **123**, 2958–2963 (2001).
9. A. M. Czyzewski, A. E. Barron, Protein and peptide biomimicry: Gold-mining inspiration from nature's ingenuity. *Aiche J.* **54**, 2–8 (2008).
10. R. J. Simon *et al.*, Peptoids: A modular approach to drug discovery. *Proc. Natl. Acad. Sci. U.S.A.* **89**, 9367–9371 (1992).
11. S. M. Miller *et al.*, Proteolytic studies of homologous peptide and N-substituted Glycine peptoid oligomers. *Bioorg. Med. Chem. Lett.* **4**, 2657–2662 (1994).
12. A. R. Statz, A. E. Barron, P. B. Messersmith, Protein, cell and bacterial fouling resistance of polypeptoid-modified surfaces: Effect of side-chain chemistry. *Soft Matter* **4**, 131–139 (2008).
13. J. E. Murphy *et al.*, A combinatorial approach to the discovery of efficient cationic peptoid reagents for gene delivery. *Proc. Natl. Acad. Sci. U.S.A.* **95**, 1517–1522 (1998).
14. B. Mojsoska, H. Jenssen, Peptides and peptidomimetics for antimicrobial drug design. *Pharmaceuticals (Basel)* **8**, 366–415 (2015).
15. W. Huang *et al.*, Learning from host-defense peptides: Cationic, amphipathic peptoids with potent anticancer activity. *PLoS One* **9**, e90397 (2014).
16. Y. Utku *et al.*, A peptidomimetic siRNA transfection reagent for highly effective gene silencing. *Mol. Biosyst.* **2**, 312–317 (2006).
17. A. M. Czyzewski *et al.*, Effective in vivo treatment of acute lung injury with helical, amphipathic peptoid mimics of pulmonary surfactant proteins. *Sci. Rep.* **8**, 6795 (2018).
18. J. Zhu *et al.*, Recent advances in anticancer peptoids. *Bioorg. Chem.* **139**, 106686 (2023).
19. Y. Gao *et al.*, Recent advances in peptoids as promising antimicrobial agents to target diverse microbial species. *Eur. J. Med. Chem.* **280**, 116982 (2024).
20. R. N. Zuckermann, J. M. Kerr, S. B. H. Kent, W. H. Moos, Efficient method for the preparation of peptoids [oligo(N-substituted glycines)] by submonomer solid-phase synthesis. *J. Am. Chem. Soc.* **114**, 10646–10647 (1992).
21. A. M. Czyzewski *et al.*, In vivo, in vitro, and in silico characterization of peptoids as antimicrobial agents. *PLoS One* **11**, e0135961 (2016).
22. N. P. Chongsiriwatana *et al.*, Peptoids that mimic the structure, function, and mechanism of helical antimicrobial peptides. *Proc. Natl. Acad. Sci. U.S.A.* **105**, 2794–2799 (2008).
23. B. Mojsoska, R. N. Zuckermann, H. Jenssen, Structure-activity relationship study of novel peptoids that mimic the structure of antimicrobial peptides. *Antimicrob. Agents Chemother.* **59**, 4112–4120 (2015).
24. A. B. Benjamin *et al.*, Efficacy of cathelicidin-mimetic antimicrobial peptoids against *Staphylococcus aureus*. *Microbiol. Spectr.* **10**, e00534-22 (2022).
25. J. E. Nielsen *et al.*, Self-assembly of antimicrobial peptoids impacts their biological effects on ESKAPE bacterial pathogens. *ACS Infect. Dis.* **8**, 533–545 (2022).
26. J. S. Lin *et al.*, Anti-persister and anti-biofilm activity of self-assembled antimicrobial peptoid ellipsoidal micelles. *ACS Infect. Dis.* **8**, 1823–1830 (2022).
27. S. J. T. Wardell *et al.*, A biofilm-targeting lipo-peptoid to treat *Pseudomonas aeruginosa* and *Staphylococcus aureus* co-infections. *Biofilm* **9**, 100272 (2025).
28. G. Diamond *et al.*, Potent antiviral activity against HSV-1 and SARS-CoV-2 by antimicrobial peptoids. *Pharmaceuticals (Basel)* **14**, 304 (2021).
29. L. Zeng *et al.*, Broad-spectrum CRISPR-mediated inhibition of SARS-CoV-2 variants and endemic coronaviruses in vitro. *Nat. Commun.* **13**, 2766 (2022).

30. A. Murayama *et al.*, Antiviral effect of peptoids on Hepatitis B virus infection in cell culture. *Antivir. Res.* **223**, 105821 (2024).
31. S. K. Mishra *et al.*, Antimicrobial activity of peptoids against metallo-beta-lactamase-producing *Klebsiella pneumoniae*, *Acinetobacter baumannii*, *Pseudomonas aeruginosa*, and other WHO priority pathogens, including *Candida auris*. *J. Appl. Microbiol.* **136**, lxaf031 (2025).
32. M. Sara *et al.*, The activity of antimicrobial peptoids against multidrug-resistant ocular pathogens. *Contact Lens Anterior Eye* **47**, 102124 (2024).
33. V. Kumar *et al.*, Membrane-acting biomimetic peptoids against visceral leishmaniasis. *FEBS Open Bio.* **13**, 519–531 (2023).
34. B. Lamont *et al.*, Antiparasitic effect of peptoids against Cryptosporidium parvum. *Microbiology (Reading)* **171**, 1–5 (2025).
35. J. Seo *et al.*, In vivo biodistribution and small animal PET of (64)Cu-labeled antimicrobial peptoids. *Bioconjug. Chem.* **23**, 1069–1079 (2012).
36. R. Kapoor *et al.*, Antimicrobial peptoids are effective against *Pseudomonas aeruginosa* biofilms. *Antimicrob. Agents Chemother.* **55**, 3054–3057 (2011).
37. N. P. Chongsiriwatana *et al.*, Short alkylated peptoid mimics of antimicrobial lipopeptides. *Antimicrob. Agents Chemother.* **55**, 417–420 (2011).
38. N. Molchanova *et al.*, Halogenation as a tool to tune antimicrobial activity of peptoids. *Sci. Rep.* **10**, 14805 (2020).
39. C. B. Park, K. S. Yi, K. Matsuzaki, M. S. Kim, S. C. Kim, Structure-activity analysis of buforin II, a histone H2A-derived antimicrobial peptide: The proline hinge is responsible for the cell-penetrating ability of buforin II. *Proc. Natl. Acad. Sci. U.S.A.* **97**, 8245–8250 (2000).
40. Y. Shai, Mode of action of membrane active antimicrobial peptides. *Biopolymers* **66**, 236–248 (2002).
41. J. D. Hale, R. E. Hancock, Alternative mechanisms of action of cationic antimicrobial peptides on bacteria. *Expert Rev. Anti Infect. Ther.* **5**, 951–959 (2007).
42. L. Otvos Jr., Antibacterial peptides and proteins with multiple cellular targets. *J. Pept. Sci.* **11**, 697–706 (2005).
43. K. A. Brogden, Antimicrobial peptides: Pore formers or metabolic inhibitors in bacteria? *Nat. Rev. Microbiol.* **3**, 238–250 (2005).
44. C. F. Le, C. M. Fang, S. D. Sekaran, Intracellular targeting mechanisms by antimicrobial peptides. *Antimicrob. Agents Chemother.* **61**, e02340-16 (2017).
45. B. Mojsoska, G. Carretero, S. Larsen, R. V. Mateiu, H. Jenssen, Peptoids successfully inhibit the growth of gram negative *E. coli* causing substantial membrane damage. *Sci. Rep.* **7**, 42332 (2017).
46. N. P. Chongsiriwatana *et al.*, Intracellular biomass flocculation as a key mechanism of rapid bacterial killing by cationic, amphipathic antimicrobial peptides and peptoids. *Sci. Rep.* **7**, 16718 (2017).
47. M. Kim *et al.*, Real-time monitoring of multitarget antimicrobial mechanisms of peptoids using label-free imaging with optical diffraction tomography. *Adv. Sci. (Weinh)* **10**, e2302483 (2023).
48. C. Y. Huang *et al.*, Lipitoids–novel cationic lipids for cellular delivery of plasmid DNA in vitro. *Chem. Biol.* **5**, 345–354 (1998).
49. V. Kesavan, N. Tamilarasu, H. Cao, T. M. Rana, A new class of RNA-binding oligomers: Peptoid amide and ester analogues. *Bioconjug. Chem.* **13**, 1171–1175 (2002).
50. J. Mao, D. Bong, Synthesis of DNA-binding peptoids. *Synlett* **26**, 1581–1585 (2015).
51. Y. Zhu, J. C. Weisshaar, M. Mustafi, Long-term effects of the proline-rich antimicrobial peptide Oncocin112 on the *Escherichia coli* translation machinery. *J. Biol. Chem.* **295**, 13314–13325 (2020).
52. Y. Zhu *et al.*, Local rigidification and possible coacervation of the *Escherichia coli* DNA by cationic nylon-3 polymers. *Biophys. J.* **120**, 5243–5254 (2021), 10.1016/j.bpj.2021.10.037.
53. H. Choi, N. Rangarajan, J. C. Weisshaar, Lights, camera, action! Antimicrobial peptide mechanisms imaged in space and time. *Trends Microbiol.* **24**, 111–122 (2016).
54. L. A. Rank *et al.*, Diverse impacts on prokaryotic and eukaryotic membrane activities from hydrophobic subunit variation among nylon-3 copolymers. *ACS Chem. Biol.* **16**, 176–184 (2021).
55. Y. Zhu, S. Mohapatra, J. C. Weisshaar, Rigidification of the *Escherichia coli* cytoplasm by the human antimicrobial peptide LL-37 revealed by superresolution fluorescence microscopy. *Proc. Natl. Acad. Sci. U.S.A.* **116**, 1017–1026 (2019).
56. M. F. Burton, P. G. Steel, The chemistry and biology of LL-37. *Nat. Prod. Rep.* **26**, 1572–1584 (2009).
57. R. Bucki, K. Leszczynska, A. Namiot, W. Sokolowski, Cathelicidin LL-37: A multitask antimicrobial peptide. *Arch. Immunol. Ther. Exp. (Warsz)* **58**, 15–25 (2010).
58. D. Vandamme, B. Landuyt, W. Luyten, L. Schoofs, A comprehensive summary of LL-37, the factotum human cathelicidin peptide. *Cell. Immunol.* **280**, 22–35 (2012).
59. K. A. Sochacki, K. J. Barns, R. Bucki, J. C. Weisshaar, Real-time attack on single Escherichia coli cells by the human antimicrobial peptide LL-37. *Proc. Natl. Acad. Sci. U.S.A.* **108**, E77–E81 (2011).
60. Y. Li *et al.*, Single-molecule visualization of dynamic transitions of pore-forming peptides among multiple transmembrane positions. *Nat. Commun.* **7**, 12906 (2016).
61. K. J. Barns, J. C. Weisshaar, Real-time attack of LL-37 on single *Bacillus subtilis* cells. *Biochim. Biophys. Acta* **1828**, 1511–1520 (2013).
62. H. Choi, Z. L. Yang, J. C. Weisshaar, Oxidative stress induced in *E. coli* by the human antimicrobial peptide LL-37. *PLoS Pathog.* **13**, e1006481 (2017).
63. E. Betzig *et al.*, Imaging intracellular fluorescent proteins at nanometer resolution. *Science* **313**, 1642–1645 (2006).
64. M. J. Rust, M. Bates, X. W. Zhuang, Sub-diffraction-limit imaging by stochastic optical reconstruction microscopy (STORM). *Nat. Methods* **3**, 793–795 (2006).
65. S. T. Hess, T. P. K. Girirajan, M. D. Mason, Ultra-high resolution imaging by fluorescence photoactivation localization microscopy. *Biophys. J.* **91**, 4258–4272 (2006).
66. H. Qian, M. P. Sheetz, E. L. Elson, Single-particle tracking - analysis of diffusion and flow in 2-Dimensional systems. *Biophys. J.* **60**, 910–921 (1991).
67. Y. Zhu, M. Mustafi, J. C. Weisshaar, Biophysical properties of *Escherichia coli* cytoplasm in stationary phase by superresolution fluorescence microscopy. *mBio* **11**, e00143-20 (2020).
68. Y. Zhu, W. E. Moerner, L. S. Qi, CRISPR-Cas-based live cell imaging of genome dynamics. *Nat. Rev. Genet.* **27** (2026), 10.1038/s41576-026-00949-z.
69. M. Joyeux, In vivo compaction dynamics of bacterial DNA: A fingerprint of DNA/RNA demixing? *Curr. Opin. Colloid Interface Sci.* **26**, 17–27 (2016).
70. X. Wang, P. Montero Ilopis, D. Z. Rudner, Organization and segregation of bacterial chromosomes. *Nat. Rev. Genet.* **14**, 191–203 (2013).
71. J. Pelletier *et al.*, Physical manipulation of the *Escherichia coli* chromosome reveals its soft nature. *Proc. Natl. Acad. Sci. U.S.A.* **109**, E2649–E2656 (2012).
72. O. Espeli, R. Mercier, F. Boccard, DNA dynamics vary according to macrodomain topography in the *E. coli* chromosome. *Mol. Microbiol.* **68**, 1418–1427 (2008).
73. S. C. Weber, A. J. Spakowitz, J. A. Theriot, Bacterial chromosomal loci move subdiffusively through a viscoelastic cytoplasm. *Phys. Rev. Lett.* **104**, 238102 (2010).
74. Y. Zhu *et al.*, High-resolution dynamic imaging of chromatin DNA communication using Oligo-LiveFISH. *Cell* **188**, 3310–3328.e27 (2025).
75. A. Javer *et al.*, Short-time movement of *E. coli* chromosomal loci depends on coordinate and subcellular localization. *Nat. Commun.* **4**, 3003 (2013).
76. C. Landon *et al.*, Real-time fluorescence microscopy on living E. coli sheds new light on the antibacterial effects of the king penguin β-defensin AvBD103b. *Int. J. Mol. Sci.* **23**, 2057 (2022).
77. M. Joyeux, Compaction of bacterial genomic DNA: Clarifying the concepts. *J. Phys. Condens. Matter* **27**, 383001 (2015).
78. V. B. Teif, K. Bohinc, Condensed DNA: Condensing the concepts. *Prog. Biophys. Mol. Biol.* **105**, 208–222 (2011).
79. S. C. Weber, A. J. Spakowitz, J. A. Theriot, Nonthermal ATP-dependent fluctuations contribute to the in vivo motion of chromosomal loci. *Proc. Natl. Acad. Sci. U.S.A.* **109**, 7338–7343 (2012).
80. S. Bakshi, H. Choi, J. Mondal, J. C. Weisshaar, Time-dependent effects of transcription- and translation-halting drugs on the spatial distributions of the *Escherichia coli* chromosome and ribosomes. *Mol. Microbiol.* **94**, 871–887 (2014).
81. S. Bakshi, H. Choi, J. C. Weisshaar, The spatial biology of transcription and translation in rapidly growing *Escherichia coli*. *Front. Microbiol.* **6**, 636 (2015).
82. S. Bakshi, A. Siryaporn, M. Goulian, J. C. Weisshaar, Superresolution imaging of ribosomes and RNA polymerase in live *Escherichiacoli* cells. *Mol. Microbiol.* **85**, 21–38 (2012).
83. Y. Zhu, Code for: Antimicrobial peptoids pass rapidly through bacterial membranes and flocculate ribosomes and DNA: A single-cell fluorescence study. Zenodo. https://doi.org/10.5281/zenodo.20727763. Deposited 17 June 2026.
84. K. A. Sochacki, I. A. Shkel, M. T. Record, J. C. Weisshaar, Protein diffusion in the periplasm of E. coli under osmotic stress. *Biophys. J.* **100**, 22–31 (2011).
85. J. G. Harrison, S. Balasubramanian, Synthesis and hybridization analysis of a small library of peptide-oligonucleotide conjugates. *Nucleic Acids Res.* **26**, 3136–3145 (1998).
86. M. Scocchi, M. Mardirossian, G. Runti, M. Benincasa, Non-membrane permeabilizing modes of action of antimicrobial peptides on bacteria. *Curr. Top. Med. Chem.* **16**, 76–88 (2016).
87. J. E. Nielsen, V. A. Bjornestad, V. Pipich, H. Jenssen, R. Lund, Beyond structural models for the mode of action: How natural antimicrobial peptides affect lipid transport. *J. Colloid Interface Sci.* **582**, 793–802 (2021).
88. M. T. Record Jr., E. S. Courtenay, D. S. Cayley, H. J. Guttman, Responses of *E. coli* to osmotic stress: Large changes in amounts of cytoplasmic solutes and water. *Trends Biochem. Sci* **23**, 143–148 (1998).
89. H. Dong, L. Nilsson, C. G. Kurland, Co-variation of tRNA abundance and codon usage in *Escherichia coli* at different growth rates. *J. Mol. Biol.* **260**, 649–663 (1996).
90. P. E. Schavemaker, W. M. Smigiel, B. Poolman, Ribosome surface properties may impose limits on the nature of the cytoplasmic proteome. *Elife* **6**, e30084 (2017).
91. J. D. Mcghee, P. H. Von hippel, Theoretical aspects of DNA-protein interactions: Co-operative and non-co-operative binding of large ligands to a one-dimensional homogeneous lattice. *J. Mol. Biol.* **86**, 469–489 (1974).
92. Y. Zhu, *Single-Cell Detection of Antimicrobial Peptide's Attack on Live E. coli by Super-Resolution Fluorescence Microscopy* (The University of Wisconsin–Madison, United States–Wisconsin, 2020), p. 239.
93. J. N. Stannard, B. L. Horecker, The in vitro inhibition of cytochrome oxidase by azide and cyanide. *Fed. Proc.* **6**, 210 (1947).
94. B. Z. Cavari, Y. Avi-dor, Effect of carbonyl cyanide m-chlorophenylhydrazone on respiration and respiration-dependent phosphorylation in *Escherichia coli*. *Biochem. J.* **103**, 601–608 (1967).
95. J. M. Kralj, D. R. Hochbaum, A. D. Douglass, A. E. Cohen, Electrical spiking in Escherichia coli probed with a fluorescent voltage-indicating protein. *Science* **333**, 345–348 (2011).
96. H. Choi, Z. Yang, J. C. Weisshaar, Single-cell, real-time detection of oxidative stress induced in *Escherichia coli* by the antimicrobial peptide CM15. *Proc. Natl. Acad. Sci. U.S.A.* **112**, E303–E310 (2015).
97. A. Thiel, M. Valens, I. Vallet-gely, O. Espeli, F. Boccard, Long-range chromosome organization in *E. coli*: A site-specific system isolates the Ter macrodomain. *PLoS Genet.* **8**, e1002672 (2012).
98. S. Bakshi, B. P. Bratton, J. C. Weisshaar, Subdiffraction-limit study of Kaede diffusion and spatial distribution in live *Escherichia coli*. *Biophys. J.* **101**, 2535–2544 (2011).
99. J. C. Crocker, D. G. Grier, Methods of digital video microscopy for colloidal studies. *J. Colloid Interface Sci.* **179**, 298–310 (1996).
100. M. Mustafi, J. C. Weisshaar, Simultaneous binding of multiple EF-Tu copies to translating ribosomes in live *Escherichia coli*. *mBio* **9**, e02143-17 (2018).
101. M. Mustafi, J. C. Weisshaar, Near saturation of ribosomal L7/L12 binding sites with ternary complexes in slowly growing *E. coli*. *J. Mol. Biol.* **431**, 2343–2353 (2019).
102. X. Michalet, Mean square displacement analysis of single-particle trajectories with localization error: Brownian motion in an isotropic medium. *Phys. Rev. E Stat. Nonlin. Soft Matter Phys.* **82**, 041914 (2010).
103. M. J. Saxton, Single-particle tracking: The distribution of diffusion coefficients. *Biophys. J.* **72**, 1744–1753 (1997).
104. M. A. Le gros, G. Mcdermott, C. A. Larabell, X-ray tomography of whole cells. *Curr. Opin. Struct. Biol.* **15**, 593–600 (2005).
105. J. R. Kremer, D. N. Mastronarde, J. R. Mcintosh, Computer visualization of three-dimensional image data using IMOD. *J. Struct. Biol.* **116**, 71–76 (1996).
106. A. Unciti-broceta, F. Diezmann, C. Y. Ou-yang, M. A. Fara, M. Bradley, Synthesis, penetrability and intracellular targeting of fluorescein-tagged peptoids and peptide-peptoid hybrids. *Bioorg. Med. Chem.* **17**, 959–966 (2009).
107. Y. Aizawa, Y. Sugiura, T. Morii, Comparison of the sequence-selective DNA binding by peptide dimers with covalent and noncovalent dimerization domains. *Biochemistry* **38**, 1626–1632 (1999).
108. J. G. Harrison, X. Liu, S. Balasubramanian, Screening for oligonucleotide binding affinity by a convenient fluorescence competition assay. *Nucleic Acids Res.* **27**, e14 (1999).